MDPI

Article

Dynamics Modeling and Load-Sharing Performance Optimization of Concentric Face Gear Split-Torque Transmission Systems

Fei Gong [1,2], Rupeng Zhu [1,2,]*, and Qibo Wang [3]

[1] National Key Laboratory of Science and Technology on Helicopter Transmission, Nanjing University of Aeronautics and Astronautics, Nanjing 210016, China; gongfei1189@163.com

[2] College of Mechanical and Electrical Engineering, Nanjing University of Aeronautics and Astronautics, Nanjing 210016, China

[3] AECC Hunan Aviation Powerplant Research Institute, Zhuzhou 412002, China

* Correspondence: rpzhu_nuaa@163.com

Abstract: The concentric face gear split-torque transmission system (CFGSTTS) has the advantages of a large reduction ratio and high power density. The CFGSTTS has considerable potential to be applied in helicopter main reducers. As such, in this study, we analyzed the load distribution characteristics of a dual input–dual output concentric face gear split-torque transmission system. A load-dependent time-varying meshing stiffness surrogate model was designed based on a feedforward neural network. The difference in the meshing stiffness between the pinion driving and face gear driving was analyzed. The coupled lumped parameter dynamic model of the bending–torsion–axis–pendulum was developed through Newton's second law, and the influences of the time-varying meshing stiffness, backlash, comprehensive transmission error, support stiffness, and damping were considered. Finally, the impact of the support stiffness on the load-sharing coefficient was analyzed. An optimization model was constructed with the objective function of minimizing the sum of the load-sharing coefficients and was solved by the marine predator algorithm. In addition, the validity of the optimization results was verified with a finite element model. The results indicate that (1) smaller support stiffnesses of input gears benefit the corresponding load balance; (2) the support stiffnesses of the face gears have different laws of influence on the load-sharing coefficient at the input gear and idler, and the support stiffnesses of the other gears need to be comprehensively considered; (3) the larger supporting stiffnesses of the idler gears and tail gear are beneficial for decreasing the load-sharing coefficient at the input gear; and (4) the optimized load-sharing coefficients at Input Gears 1 and 2 and the idler gear decrease by 23.7%, 24.2%, and 4.6%, respectively.

Keywords: concentric face gear; split torque; surrogate model; load sharing; optimization

1. Introduction

The performance of drive systems has a substantial impact on rotorcrafts. New transmission configurations are being proposed and developed to meet the high power-to-weight ratio and high reliability requirements of helicopter main gearbox transmission systems. White [1] proposed an alternative design solution for planetary transmissions called a split-torque design. Kish [2] and Krantz [3,4] concluded that the split-torque design can reduce the weight and has notable advantages over conventional designs. However, the problem remains as to how to ensure the loads are equal across the branches. Therefore, a series of projects funded by the National Aeronautics and Space Administration (NASA) [2,5–9], which started in the 1980s, has conducted considerable research on cylindrical gear power-split drives and power-split transmissions containing face gears. Moreover, the cylindrical split-torque transmission and the face gear split-torque transmission were successfully applied to the Comanche [10] and Block III [11] helicopter drive systems.

A critical piece of technology regarding split-torque transmissions is their equal-load design, which indicates that the loads borne in the split-torque path are as equal as possible [12]. If loads are not equal, the gears carrying larger loads are prone to excessive wear and even failure. Therefore, torque equality between different paths is a crucial topic in the design of split-torque transmissions. Scholars worldwide have extensively studied the technical requirements of load equalization in the split-torque design of cylindrical gears and face gears.

The load-sharing mechanisms, statics, and dynamics of cylindrical gear split-torque have aspects studied. Krantz [4] demonstrated that improved load-sharing performance can be achieved through proper structural designs, which can reduce dynamic transmission errors and noise, and analyzed the dynamics of a split-torque gear system. Then, Zhao et al. [13] created a dynamic model of a power-split transmission, solved the motion equations using the numerical integration method, and considered how the interaction of internal parameters affects load sharing. Additionally, Dong et al. [14] obtained time-varying meshing stiffness curves through loaded tooth contact analysis and set up a quasi-static model of a power-split gear train to determine the load-sharing ratios for different installation errors. Fu et al. [15] modeled the nonlinear dynamics of a power-split drive system for helicopters, evaluated the load-sharing features using dynamic analysis, and improved the load-averaging performance by modifying the phase difference based on an enhanced NSGA-II optimization algorithm. Dong et al. [16] constructed a static model for a power-split star gear drive containing spur and helical gears to examine the influences of machining errors, mounting errors, and component floats on the load distribution factor. Moreover, Hu et al. [17] developed a two-path split-torque gear system dynamics model to analyze the natural frequency, critical speed, dynamic relative displacement of gear pairs, and load distribution characteristics. The model considered nonlinear factors, such as tooth clearance, transmission errors, and gyroscopic effects. Furthermore, Liu et al. [18] analyzed loaded and unloaded tooth meshing to obtain the time-varying meshing stiffness and then constructed a dynamics model of a dual-input two-path power-sharing transmission system considering meshing errors. Then, the effects of tooth modifications on the load distributions and dynamic load characteristics were explored. A three-dimensional analysis model of a two-power-input split-torque gear drive with 41 degrees of freedom was created by Jin et al. [19,20] using the centralized parameter method. The system response was obtained using the Fourier series method, which revealed the law of the variation in the friction torque coefficient and friction stiffness, as well as the impact of harmonic frequency on the transmission error.

The face gear drive has the advantages of a high reduction ratio, low error sensitivity, and simple support structure, compared with cylindrical gears and spiral bevel gears, and is primarily utilized in split-torque transmissions for helicopter main gearboxes [6,21]. With the support of the Advanced Rotorcraft Transmission (ART) Program, Litvin studied tooth geometry designs [22,23], tooth contact analysis methods [23], modifications [24], and grinding [25] for face gear drives. The suitability of face gears for high rotational speed and heavy load transmissions was fully verified, both theoretically and experimentally, in the middle and late stages of the ART program [26,27]. Moreover, various split-torque configurations containing face gears [5,28,29] have been proposed, and their load-sharing and dynamic characteristics have been thoroughly investigated. Additionally, Handschuh et al. [27] tested six sets of face gears with different geometries and different heat treatments to evaluate the feasibility of face gears in the main helicopter rotor gearboxes and to identify the failure mechanisms and load-carrying capability in a simulated helicopter transmission environment. Pias et al. [28] designed a split-power drive system with two face gears. The input pinion with a floating structure meshed with two coaxial counterrotating face gears. Moreover, Jin et al. [29] proposed a quadratic split-power transmission system containing face gears. The trends in load distribution and dynamic load coefficients with tooth clearances were studied using numerical methods. Mo et al. [30] examined a face gear split-power system with manufacturing and assembly errors using

the lumped parameter model and developed a translational–torsional coupling model. An analysis of the dynamic factors' influence on the load distribution coefficient revealed that the load on the gears might be more equally distributed by adjusting the dynamic parameters. Mo et al. [31] created differential equations of a two-input face gear transmission. The impacts of the eccentricity error, support stiffness, and torsional stiffness were estimated on the contact force and sharing between gear pairs. Dong et al. [32] formed dynamic differential equations of a coaxial face gear drive that considered the time-varying mesh stiffness, backlash, and other factors. Moreover, the change in the load-sharing behavior under different parameters was analyzed. Zhao et al. [33] investigated the load-sharing behavior of a coaxial split-torque face gear train by using a combination of lumped parameters and finite elements. The analysis showed that the matching design of the backlash and support stiffness and an even number of pinion teeth can improve the system load distribution performance. Dong et al. [34] explored the natural properties of the face gear power-split train and described the effect of the torsional flexibility of the input gear shaft on the dynamic load distribution.

The above scholars' ongoing research has considerably advanced our understanding of dynamic gear load-sharing properties and dynamic response. However, few have modeled the load-dependent time-varying mesh stiffness of face gears and considered it in the dynamics of the CFGSTTS. Moreover, few researchers have optimized the dynamic load-sharing features of the CFGSTTS.

Therefore, in this study and based on the existing research, a more accurate dynamic load-sharing analysis model for the CFGSTTS was constructed using the centralized parameters method. The model considered the load-dependent time-varying meshing stiffness and two different meshing states, the pinion driving and the face gear driving, backlash, support stiffness, and other factors. Then, dynamic differential equations were solved by the numerical integration method, and the law of the variation in the load-sharing factor with the input load and support stiffness was obtained. Finally, taking the minimum sum of load-sharing factors as the objective function, a load-sharing optimization model of the CFGSTTS was developed using the marine predator optimization algorithm. Then, the change direction of the support stiffness under the optimal solution was obtained.

2. Modeling

The CFGSTTS shown in Figure 1 consists of two face gears and five pinions, and the five pinions are two input gears, two idler gears, and one tail gear. Moreover, the power flow direction [35] is shown in Figure 2. The power enters from the input gear and is transferred partly to the upper face gear and partly to the lower face gear. Hence, the input gear is the driving gear, as shown in Figure 2a. In contrast, the idlers are driven by the lower face gear and transmit the power to the upper face gear. The lower face gear also drives the tail gear, and its transmitted power is partly transmitted to the upper face gear and partly output to the intermediate reducer. Therefore, among the ten gear pairs of the system, Idler 1, Idler 2, and the tail gear are driven by the lower face gear. The meshing state of these three gear pairs is different from the rest.
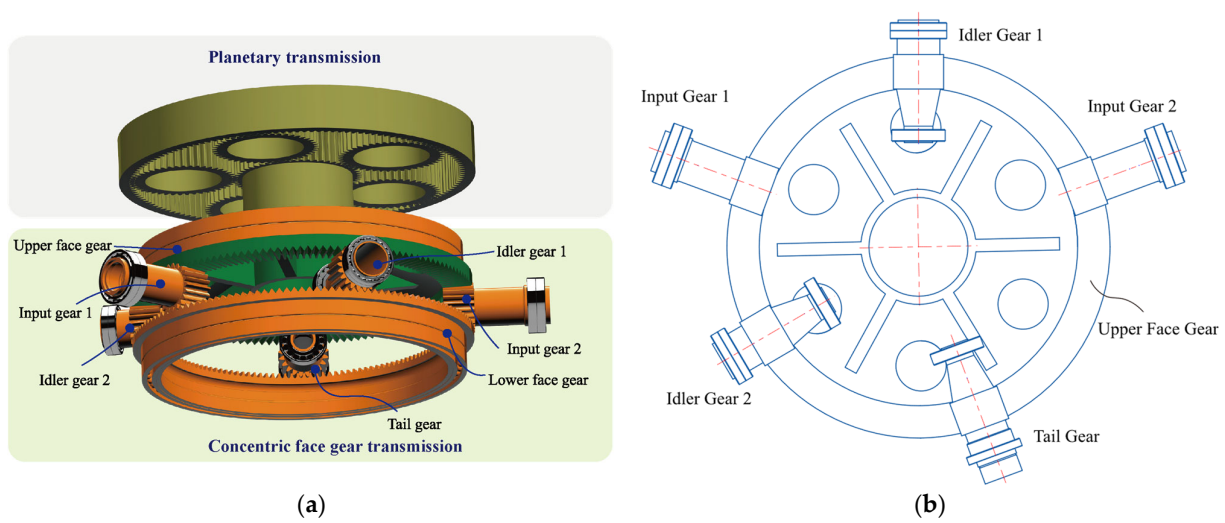
Figure 1. Schematic diagram of concentric face gear split-torque transmission system: (**a**) 3D schematic diagram; (**b**) 2D schematic diagram.
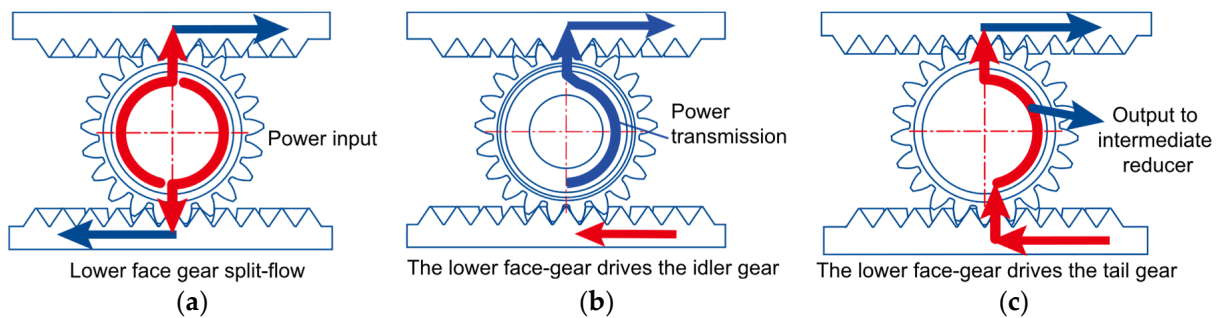

Figure 2. Power flow direction of CFGSTTS: (**a**) input gear; (**b**) idler gear; (**c**) tail gear.

## 2.1. Neural Network Surrogate Models for Time-Varying Mesh Stiffnesses

The mesh of the face gear and pinion is a nonconjugate contact, where the contact position is a point that expands into an elliptical contact area with respect to the magnitude of the load when bearing the load. Moreover, as the load increases, the number of teeth simultaneously engaged in the face gear mesh pair increases, and the shape of the mesh stiffness curve changes. Therefore, the mesh stiffness pair is closely related to the load. In the CFGSTTS, the elastic support stiffness of the gears affects the load distribution among the gears. The elastic support stiffness changes, and the normal contact force of the gear pair changes accordingly, leading to a change in the mesh stiffness. Consequently, a load-dependent time-varying meshing stiffness model was developed to further consider the time-varying meshing stiffness.

In our previous study, we used the strain energy approach to determine the mesh stiffness [35]. The upper face gear contains the web. The face gear's parameters are listed in Table 1. The specific loading and simulation procedure is described in the literature [35]. Notably, in this study, the contact stiffness of the tooth contact pair was set to 10 times the default value, which was 1.0; the convergence tolerances of the displacement and force were set to 1/100 of the default values, which were 0.05 and 0.005, respectively. The computational cost increased, but a smoother mesh stiffness curve could be acquired.

Table 1. Main design parameters of face gear pair.

Parameter	Pinion	Face Gear
Number of teeth	21	142
Normal modulus (mm)	3.9	3.9
Pressure angle (deg)	25	25
Tooth width (mm)	51	49

Through quasistatic finite element analysis, the meshing stiffness data, including the load, pinion rotation angle, and stiffness values, were obtained for 1 cycle under 42 sets of loads in the range of 100 to 8000 Nm. Surrogate models can be used to quickly provide a solution instead of a real system by seeking the response relationship between the input and output variables. For complex nonlinear problems, the multilayer feedforward neural network is a more commonly used surrogate model. A multilayer feedforward neural network is a network model with a hierarchical structure composed of simple neural units, which has a strong simulation ability for nonlinear systems. In this study, 42 sets of data were used as training samples to construct a neural network with the topology shown in Figure 3, including input, hidden, and output layers. The input layer contained two neurons corresponding to the load and pinion angle, and the output layer was one neuron corresponding to the meshing stiffness value; in addition, the number of neurons in the 2 hidden layers was 20 and 5, respectively. The meshing stiffness neural network models of the lower and upper face gears after training are visualized in Figures 4a and 5a, respectively.
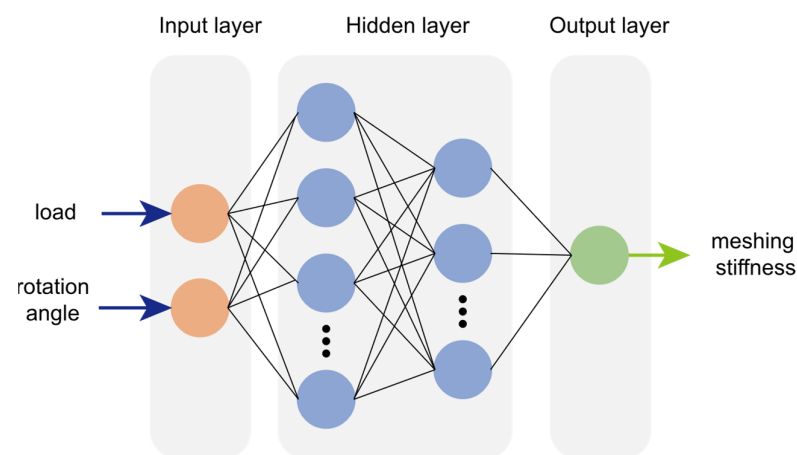
Figure 3. Multilayer feedforward neural network topology.
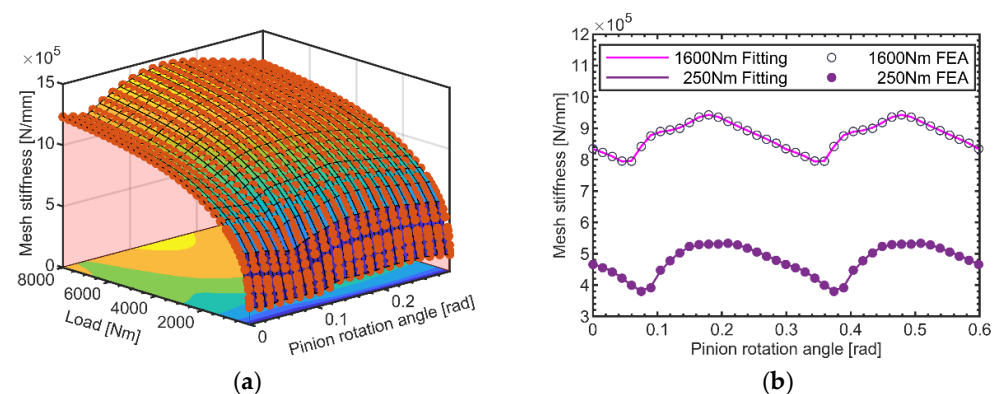
Figure 4. Mesh stiffness model of the lower face gear: (**a**) neural network model; (**b**) verification of generalization capability.
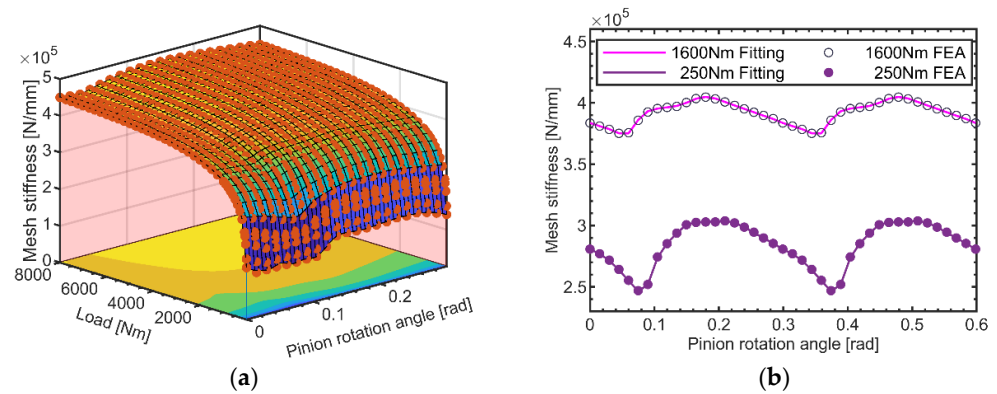
Figure 5. Mesh stiffness model of upper face gear: (**a**) neural network model; (**b**) verification of generalization capability.

The generalization ability of feedforward neural networks refers to the ability of the network to describe the correct input–output relationship for nontrained samples in the same sample set, which is used to characterize the prediction ability of the learning model for unknown data. To verify the generalization ability of the load-related time-varying mesh stiffness proxy model, the prediction values of the neural network were calculated for input loads of 250 and 1600 Nm. The results in Figures 4b and 5b show that the output of the agent model was almost the same as that of the finite element simulation, indicating that the agent model had a strong generalization capability.

Figure 6 illustrates the meshing stiffness at a fixed load and the meshing stiffness as a function of the load. With the support stiffness shown in Table 2, the static meshing forces of Input Gear 1 with the lower and upper face gears were 8967 and 12,588 N, respectively. Furthermore, based on this meshing force, the meshing stiffness of Input Gear 1 with the lower face gear Kh16g and the upper face gear Kh17g was calculated for a given load. Kh16 and Kh17 are the meshing stiffnesses calculated based on the meshing stiffness proxy model. Figure 6 shows that Kh16 is different from Kh16g and that Kh17 and Kh17g differ in value. The dynamic meshing forces of gear pairs of Input Gear 1 were calculated, as shown in Figure 7a,b, with load-fixed and load-related meshing stiffness. In Figure 7a, Fn16g has more frequency components and a smaller average meshing force than Fn16. The minimum values of meshing forces Fn17 and Fn17g were 12,228 and 12,124 N, respectively, and the average values were 14,744 and 14,645 N, respectively. The load-sharing coefficients obtained by Formula (38) were 1.368 and 1.376 under load-related and load-fixed meshing stiffness, respectively. Therefore, associating the meshing stiffness with the load is beneficial to increasing the accuracy of the model of CFGSTTS dynamics.
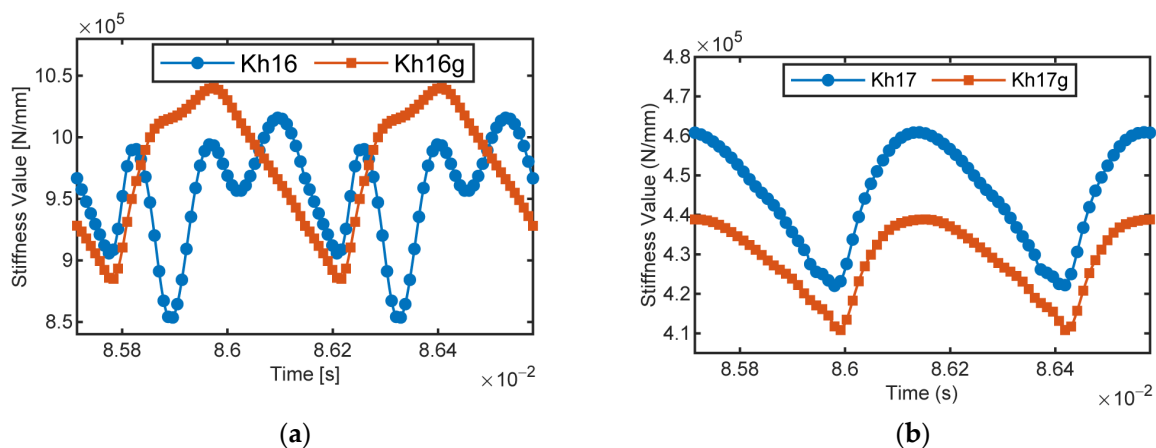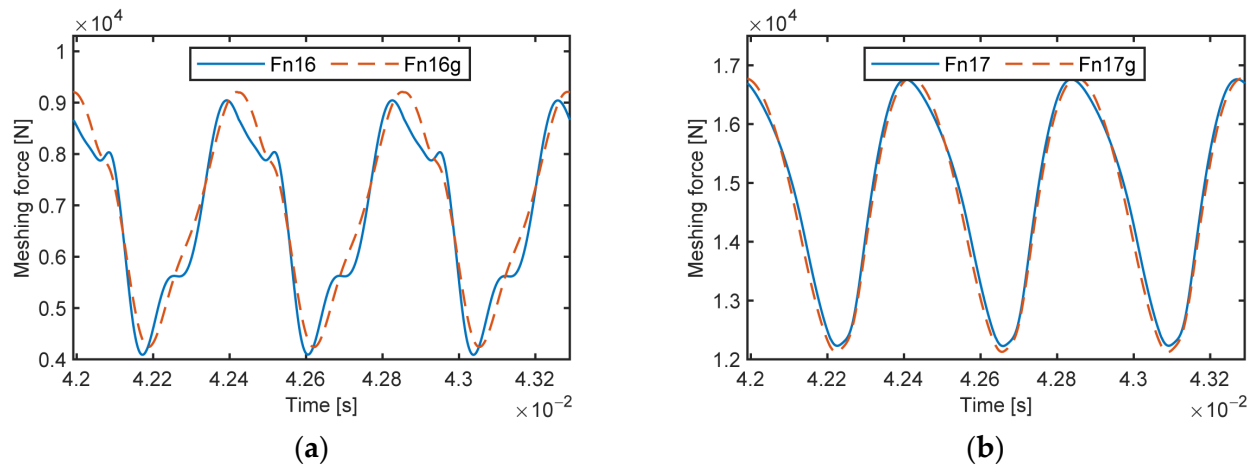

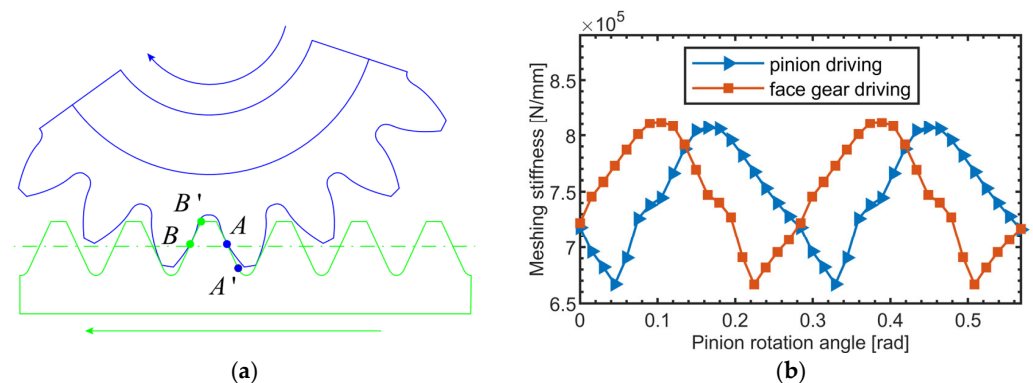**Figure 6.** Difference in meshing stiffness between fixed and varying load: (**a**) lower face gear; (**b**) upper face gear.

Table 2. Values of gear support stiffness.

	k_x (N/mm)	k_y (N/mm)	k_z (N/mm)	$k_{\theta x}$ (Nmm/rad)	$k_{\theta y}$ (Nmm/rad)
Input gear	4.0×10^5	4.0×10^5	/	/	/
Idler gear	9.4×10^5	9.4×10^5	/	/	/
Tail gear	7.7×10^5	7.7×10^5	/	/	/
Upper face gear	3.2×10^6	3.2×10^6	1.8×10^6	4.8×10^{10}	4.8×10^{10}
Lower face gear	1.5×10^7	1.5×10^7	1.26×10^7	3.2×10^{11}	3.2×10^{11}

Figure 7. Difference in meshing force between fixed and varying load: (**a**) lower face gear; (**b**) upper face gear.

2.2. Two Types of Meshing States

The meshing process of the same meshing pair driven by the face gear and pinion is shown in Figure 8a. The tooth profile of face gear in Figure 8a is at the midpoint of the tooth width. Assuming that the middle plane of the pinion groove coincides with the middle plane of the face gear tooth, two meshing points, A and B, simultaneously exist on both teeth faces of the face gear if the clearance is not considered. If the pinion drives the face gear to rotate clockwise, the meshing point A moves toward A′ at the root of the face gear. Conversely, if the face gear drives the pinion to rotate clockwise, meshing point B gradually moves toward B′ at the tip of the face gear. The corresponding mesh stiffness curves are shown in Figure 8b. The figure shows that the two curves differ not only in phase, but also in curve direction. The meshing stiffness of the pinion-driving gear pair is denoted as $k(t)$; then, the meshing stiffness of the face gear-driving meshing pair is denoted as $\widetilde{k}(t+\widetilde{t})$, where $\widetilde{k}$ is the inverse of $k(t)$, and $\widetilde{t}$ is the phase difference.

Figure 8. Difference in meshing stiffness between face gear driving and pinion driving: (**a**) direction of meshing; (**b**) difference in meshing stiffness.

Due to nonlinear excitation, a face gear may have three contact states during the transmission process: regular meshing, disengagement, and tooth-back contact. In the dynamic studies of the face gear drive [12,35], the meshing stiffness of the tooth-back mesh has not been differentiated from that of the regular mesh. Therefore, in this study, based on the meshing stiffness agent model, the meshing model considering the disengagement and tooth-back contact was established, denoted as:

$$K(f_\delta, t) = \begin{cases} k_1(t), f_\delta > 0 \\ 0, f_\delta = 0 \\ k_2(t), f_\delta < 0 \end{cases} \tag{1}$$

where $k_1(t)$ is the meshing stiffness for regular meshing, $k_2(t)$ is the meshing stiffness for tooth-back meshing, and f_δ is the relative displacement of the gear pair.

In the coaxial face gear split-torque transmission system, the distribution of the pinion around the circumference of the face gear and the difference in the number of pinion teeth may introduce meshing phase differences among the different meshing pairs. Figure 8a shows the initial meshing state of Input Gear 1 with the lower face gear, and the meshing stiffness for one cycle was calculated from this starting position and is expressed as $k_{in1\text{-}L} = k(t)$. When the number of pinion teeth is even, no phase difference exists among the meshing pairs driven by the pinion. When the number of pinion teeth is odd, the phase difference between the rest of the meshing pairs and the Input Gear 1–lower face gear meshing pair is determined with the following method:

(a) If pinion M and Input Gear 1 are distributed on the circumference of the lower face gear differing by n (n is an integer) face gear teeth, then the phase difference between the meshing stiffness $k_{M\text{-}L}$ and $k_{in1\text{-}L}$ is 0. In contrast, the phase difference between the meshing stiffness $k_{M\text{-}U}$ and $k_{in1\text{-}L}$ is T/2, where T is the meshing period.

(b) If the pinion M and Input Gear 1 are distributed on the circumference of the lower face gear differing by $n + 1/2$ face gear teeth, then the phase difference between the meshing stiffness $k_{M\text{-}L}$ and $k_{in1\text{-}L}$ is T/2. At this time, the phase difference between $k_{M\text{-}U}$ and $k_{in1\text{-}L}$ is 0.

2.3. Nonlinear Dynamic Model

The arrangement of pinions on the circumference of the face gear and the position of the face gear in space is illustrated in Figures 9 and 10, respectively. Figures 9 and 10 show the local coordinate system representing the direction of the DOFs of each gear. The x- and y-axis of the pinion are radial, the z-axis is axial, and the y-axis points to the upper face gear. The y-axis of the face gear is parallel to the axis of Idler 1 and points in the negative direction of z_3. The z-axis of the upper face gear is in the same direction as the z-axis of the lower face gear.

According to the principle of the meshing transmission between the orthogonal face gear and pinion, the meshing force can be decomposed into the radial and circumferential forces on the pinion and the axial and circumferential forces on the face gear. The pinion is not subjected to axial component force, which simplifies the support structure of the system and reduces the degrees of freedom of vibration. Accordingly, two radial degrees of freedom, x and y, and a torsional degree of freedom around the axis of the pinion were considered in this study. In the CFGSTTS, the face gear simultaneously meshes with five pinions. The nonuniform distribution of the pinions on the circumference of the face gear and the difference in the support stiffness of each gear result in the meshing force transmitted by each pinion being different. As a result, the face gears are subjected to time-varying overturning moments. Therefore, the face gear model considers six degrees of freedom. The dynamics model of the concentric face gear split-torque transmission system is shown in Figure 11.
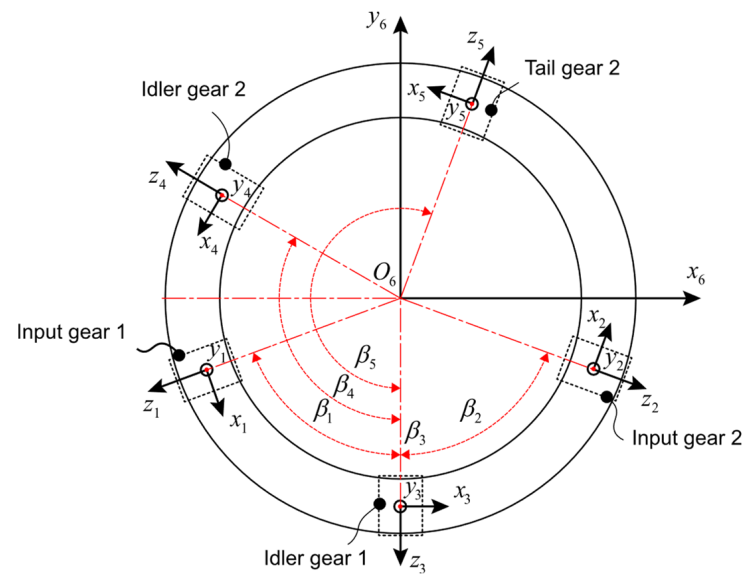
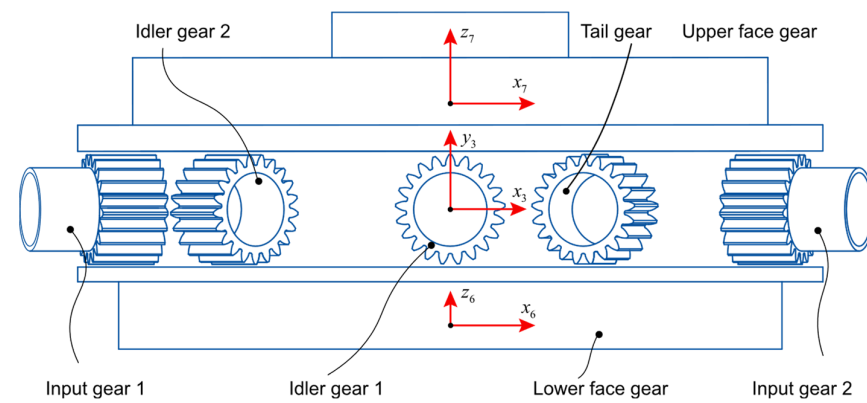**Figure 9.** Distribution of pinions around circumference of face gear.

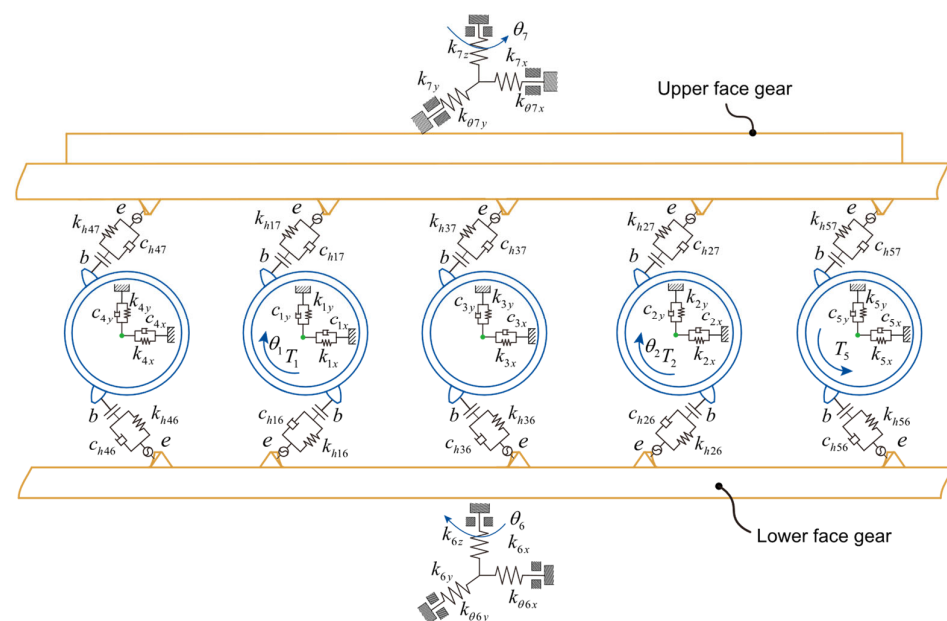**Figure 10.** Distribution of face gears.

Figure 11. Dynamics model of concentric face gear split-torque transmission system.

Under the action of external driving torque and internal excitation, the meshing point of the face gear and pinion deforms and vibrates along the meshing line. The relative displacement δ_{16} of the meshing point between Input Gear 1 and the lower face gear pair in the direction of the meshing line is expressed as:

$$\delta_{16} = \left(r_1\theta_1 - r_f\theta_6 - X_1 + X_6\cos\beta_1 - Y_6\sin\beta_1\right)\cos\alpha + (Z_6 - Y_1)\sin\alpha + \Delta\epsilon_{16} - e_{16} \quad (2)$$

where α is the pressure angle; β_1 is the pinion distribution angle; r_1 and r_f are the distances from the meshing point to the pinion and face gear axes, respectively; and e_{16} is the normal static transmission error of the gear pair, which is obtained from Equation (3).

$$e(t) = e_0 + e_r\cos(\omega_h t + \varphi_r) \quad (3)$$

where e_0 is the constant value of the comprehensive transmission error; e_r is the amplitude; ω_h is the meshing angular frequency of the gear pair; and φ_r is the initial phase.

$\Delta\epsilon_{16}$ is the relative displacement formed by the rotation of the lower face gear along x_6 and y_6, expressed as:

$$\Delta\epsilon_{16} = -r_f\sin\theta_{6x}\cos\beta_1\sin\alpha + r_f\sin\theta_{6y}\sin\beta_1\sin\alpha \quad (4)$$

Likewise, the relative displacement δ_{17} of the meshing point between Input Gear 1 and the upper face gear in the meshing line direction is expressed as:

$$\delta_{17} = \left(r_1\theta_1 - r_f\theta_{7z} + X_1 - X_7\cos\beta_1 + Y_7\sin\beta_1\right)\cos\alpha + (Y_1 - Z_7)\sin\alpha + \Delta\epsilon_{17} - e_{17} \quad (5)$$

$$\Delta\epsilon_{17} = r_f sin\theta_{7x}\cos\beta_1\sin\alpha - r_f sin\theta_{7y}\sin\beta_1\sin\alpha \quad (6)$$

Similarly, the relative displacements δ_{26} and δ_{27} of Input Gear 2 with the lower and upper face gears in the direction of the meshing line, respectively, are:

$$\delta_{26} = \left(r_2\theta_2 - r_f\theta_{6z} - X_2 + X_6\cos\beta_2 - Y_6\sin\beta_2\right)\cos\alpha + (Z_6 - Y_2)\sin\alpha + \Delta\epsilon_{26} - e_{26} \quad (7)$$

$$\delta_{27} = \left(r_2\theta_2 - r_f\theta_{7z} + X_2 - X_7\cos\beta_2 + Y_7\sin\beta_2\right)\cos\alpha + (Y_2 - Z_7)\sin\alpha + \Delta\epsilon_{27} - e_{27} \quad (8)$$

$$\Delta\epsilon_{26} = -r_f\sin\theta_{6x}\cos\beta_2\sin\alpha - r_f\sin\theta_{6y}\sin\beta_2\sin\alpha \quad (9)$$

$$\Delta\epsilon_{27} = r_f\sin\theta_{7x}\cos\beta_2\sin\alpha + r_f\sin\theta_{7y}\sin\beta_2\sin\alpha \quad (10)$$

The relative displacements δ_{36} and δ_{37} of Idler 1 with the lower and upper face gears in the direction of the meshing line, respectively, are:

$$\delta_{36} = \left(r_f\theta_6 - r_3\theta_3 + X_3 - X_6\cos\beta_3 + Y_6\sin\beta_3\right)\cos\alpha + (Z_6 - Y_3)\sin\alpha + \Delta\epsilon_{36} - e_{36} \quad (11)$$

$$\delta_{37} = \left(r_3\theta_3 - r_f\theta_{7z} + X_3 - X_7\cos\beta_3 + Y_7\sin\beta_3\right)\cos\alpha + (Y_3 - Z_7)\sin\alpha + \Delta\epsilon_{37} - e_{37} \quad (12)$$

$$\Delta\epsilon_{36} = -r_f\sin\theta_{6x}\cos\beta_3\sin\alpha + r_f\sin\theta_{6y}\sin\beta_3\sin\alpha \quad (13)$$

$$\Delta\epsilon_{37} = r_f\sin\theta_{7x}\cos\beta_3\sin\alpha - r_f\sin\theta_{7y}\sin\beta_3\sin\alpha \quad (14)$$

The relative displacements δ_{46} and δ_{47} of Idler 2 with the lower and upper face gears in the direction of the meshing line, respectively, are:

$$\delta_{46} = \left(r_f \theta_{6z} - r_4 \theta_4 + X_4 - X_6 \cos \beta_4 + Y_6 \sin \beta_4 \right) \cos \alpha + (Z_6 - Y_4) \sin \alpha + \Delta \epsilon_{46} - e_{46} \quad (15)$$

$$\delta_{47} = \left(r_4 \theta_4 - r_f \theta_{7z} + X_4 - X_7 \cos \beta_4 + Y_7 \sin \beta_4 \right) \cos \alpha + (Y_4 - Z_7) \sin \alpha + \Delta \epsilon_{47} - e_{47} \quad (16)$$

$$\Delta \epsilon_{46} = -r_f \sin \theta_{6x} \cos \beta_4 \sin \alpha + r_f \sin \theta_{6y} \sin \beta_4 \sin \alpha \quad (17)$$

$$\Delta \epsilon_{47} = r_f \sin \theta_{7x} \cos \beta_4 \sin \alpha - r_f \sin \theta_{7y} \sin \beta_4 \sin \alpha \quad (18)$$

The relative displacements δ_{56} and δ_{57} of the tail gear with the lower and upper face gears in the direction of the meshing line, respectively, are:

$$\delta_{56} = \left(r_f \theta_{6z} - r_5 \theta_5 + X_5 - X_6 \cos \beta_5 + Y_6 \sin \beta_5 \right) \cos \alpha + (Z_6 - Y_5) \sin \alpha + \Delta \epsilon_{56} - e_{56} \quad (19)$$

$$\delta_{57} = \left(r_5 \theta_5 - r_f \theta_{7z} + X_5 - X_7 \cos \beta_5 + Y_7 \sin \beta_5 \right) \cos \alpha + (Y_5 - Z_7) \sin \alpha + \Delta \epsilon_{57} - e_{57} \quad (20)$$

$$\Delta \epsilon_{56} = -r_f \sin \theta_{6x} \cos \beta_5 \sin \alpha + r_f \sin \theta_{6y} \sin \beta_5 \sin \alpha \quad (21)$$

$$\Delta \epsilon_{57} = r_f \sin \theta_{7x} \cos \beta_5 \sin \alpha - r_f \sin \theta_{7y} \sin \beta_5 \sin \alpha \quad (22)$$

The dynamic load of the gear pair in the direction of the meshing line is obtained from Equation (23).

$$F_n = k(t) f(\delta) + c_m \dot{\delta} \quad (23)$$

where $k(t)$ is the time-varying meshing stiffness; δ is the relative displacement of the meshing point; $\dot{\delta}$ is the relative velocity; and c_m is the meshing damping.

The expression of the nonlinear backlash function $f(\delta)$ is shown in Equation (24), where b is half of the backlash; its function graph is shown in Figure 12.
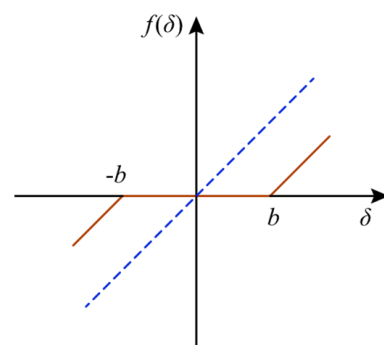

Figure 12. Schematic diagram of backlash function.

$$f(\delta) = \begin{cases} \delta - b, \delta > b \\ 0, -b < \delta < b \\ \delta + b, \delta < -b \end{cases} \quad (24)$$

c_m is the meshing damping, which is expressed as:

$$c_m = 2\xi \sqrt{k_{av} \left(1/m_{eq,p} + 1/m_{eq,f} \right)} \quad (25)$$

where ξ is the mesh damping ratio, generally taken as 0.03~0.17; k_{av} is the mean mesh stiffness; and $m_{eq,i}$ is the equivalent mass of the gear.

Then, according to Newton's second law, the differential equation of vibration of Input Gear 1 is:

$$\begin{cases} m_1\ddot{X}_1 + c_{1x}\dot{X}_1 + k_{1x}X_1 = F_{16}\cos\alpha - F_{17}\cos\alpha \\ m_1\ddot{Y}_1 + c_{1y}\dot{Y}_1 + k_{1y}Y_1 = F_{16}\sin\alpha - F_{17}\sin\alpha \\ J_1\ddot{\theta}_1 = T_1 - F_{16}r_1\cos\alpha - F_{17}r_1\cos\alpha \end{cases} \tag{26}$$

Similarly, the differential equation for the vibration of Input Gear 2 is:

$$\begin{cases} m_2\ddot{X}_2 + c_{2x}\dot{X}_2 + k_{2x}X_2 = F_{26}\cos\alpha - F_{27}\cos\alpha \\ m_2\ddot{Y}_2 + c_{2y}\dot{Y}_2 + k_{2y}Y_2 = F_{26}\sin\alpha - F_{27}\sin\alpha \\ J_2\ddot{\theta}_2 = T_2 - F_{26}r_2\cos\alpha - F_{27}r_2\cos\alpha \end{cases} \tag{27}$$

The differential equation for the vibration of Idler 1 is:

$$\begin{cases} m_3\ddot{X}_3 + c_{3x}\dot{X}_3 + k_{3x}X_3 = -F_{36}\cos\alpha - F_{37}\cos\alpha \\ m_3\ddot{Y}_3 + c_{3y}\dot{Y}_3 + k_{3y}Y_3 = F_{36}\sin\alpha - F_{37}\sin\alpha \\ J_3\ddot{\theta}_3 = F_{36}r_3\cos\alpha - F_{37}r_3\cos\alpha \end{cases} \tag{28}$$

The differential equation for the vibration of Idler 2 is:

$$\begin{cases} m_4\ddot{X}_4 + c_{4x}\dot{X}_4 + k_{4x}X_4 = -F_{46}\cos\alpha - F_{47}\cos\alpha \\ m_4\ddot{Y}_4 + c_{4y}\dot{Y}_4 + k_{4y}Y_4 = F_{46}\sin\alpha - F_{47}\sin\alpha \\ J_4\ddot{\theta}_4 = F_{46}r_4\cos\alpha - F_{47}r_4\cos\alpha \end{cases} \tag{29}$$

The differential equation for the vibration of the tail gear is:

$$\begin{cases} m_5\ddot{X}_5 + c_{5x}\dot{X}_5 + k_{5x}X_5 = -F_{56}\cos\alpha - F_{57}\cos\alpha \\ m_5\ddot{Y}_5 + c_{5y}\dot{Y}_5 + k_{5y}Y_5 = F_{56}\sin\alpha - F_{57}\sin\alpha \\ J_5\ddot{\theta}_5 = F_{56}r_5\cos\alpha - F_{57}r_5\cos\alpha - T_5 \end{cases} \tag{30}$$

The differential equation for the vibration of the lower face gear is:

$$\begin{cases} m_6\ddot{X}_6 + c_{6x}\dot{X}_6 + k_{6x}X_6 = \begin{pmatrix} -F_{16}\cos\beta_1 - F_{26}\cos\beta_2 \\ +F_{36}\cos\beta_3 + F_{46}\cos\beta_4 + F_{56}\cos\beta_5 \end{pmatrix}\cos\alpha \\ m_6\ddot{Y}_6 + c_{6y}\dot{Y}_6 + k_{6y}Y_6 = \begin{pmatrix} F_{16}\sin\beta_1 - F_{26}\sin\beta_2 - F_{36}\sin\beta_3 \\ -F_{46}\sin\beta_4 - F_{56}\sin\beta_5 \end{pmatrix}\cos\alpha \\ m_6\ddot{Z}_6 + c_{6z}\dot{Z}_6 + k_{6z}Z_6 = (-F_{16} - F_{26} - F_{36} - F_{46} - F_{56})\sin\alpha \\ J_{6x}\ddot{\theta}_{6x} + c_{\theta6x}\dot{\theta}_{6x} + k_{\theta6x}\theta_{6x} = \begin{pmatrix} F_{16}\cos\beta_1 + F_{26}\cos\beta_2 + F_{36}\cos\beta_0 \\ +F_{46}\cos\beta_4 + F_{56}\cos\beta_5 \end{pmatrix}r_f\cos\theta_{6x}\sin\alpha \\ J_{6y}\ddot{\theta}_{6y} + c_{\theta6y}\dot{\theta}_{6y} + k_{\theta6y}\theta_{6y} = \begin{pmatrix} -F_{16}\sin\beta_1 + F_{26}\sin\beta_2 \\ -F_{36}\sin\beta_0 - F_{46}\sin\beta_4 - F_{56}\sin\beta_5 \end{pmatrix}r_f\cos\theta_{6y}\sin\alpha \\ J_{6z}\ddot{\theta}_{6z} = (F_{16} + F_{26} - F_{36} - F_{46} - F_{56})r_f\cos\alpha \end{cases} \tag{31}$$

The differential equation for the vibration of the upper face gear is:

$$\begin{cases} m_7\ddot{X}_7 + c_{7x}\dot{X}_7 + k_{7x}X_7 = \begin{pmatrix} F_{17}\cos\beta_1 + F_{27}\cos\beta_2 \\ +F_{37}\cos\beta_3 + F_{47}\cos\beta_4 + F_{57}\cos\beta_5 \end{pmatrix}\cos\alpha \\ m_7\ddot{Y}_7 + c_{7y}\dot{Y}_7 + k_{7y}Y_7 = \begin{pmatrix} -F_{17}\sin\beta_1 + F_{27}\sin\beta_2 \\ -F_{37}\sin\beta_3 - F_{47}\sin\beta_4 - F_{57}\sin\beta_5 \end{pmatrix}\cos\alpha \\ m_7\ddot{Z}_7 + c_{7z}\dot{Z}_7 + k_{7z}Z_7 = (F_{17} + F_{27} + F_{37} + F_{47} + F_{57})\sin\alpha \\ J_{7x}\ddot{\theta}_{7x} + c_{\theta7x}\dot{\theta}_{7x} + k_{\theta7x}\theta_{7x} = \begin{pmatrix} -F_{17}\cos\beta_1 - F_{27}\cos\beta_2 \\ -F_{37}\cos\beta_0 - F_{47}\cos\beta_4 - F_{57}\cos\beta_5 \end{pmatrix}r_f\cos\theta_{7x}\sin\alpha \\ J_{7y}\ddot{\theta}_{7y} + c_{\theta7y}\dot{\theta}_{7y} + k_{\theta7y}\theta_{7y} = \begin{pmatrix} F_{17}\sin\beta_1 - F_{27}\sin\beta_2 \\ +F_{37}\sin\beta_0 + F_{47}\sin\beta_4 + F_{57}\sin\beta_5 \end{pmatrix}r_f\cos\theta_{7y}\sin\alpha \\ J_{7z}\ddot{\theta}_{7z} = (F_{17} + F_{27} + F_{37} + F_{47} + F_{57} - T_7)r_f\cos\alpha \end{cases} \tag{32}$$

2.4. Optimization Model Based on MPA

The marine predator algorithm (MPA) is a novel swarm optimization algorithm that was proposed by Faramarzi et al. [36]. The core of this algorithm is a combination of three different foraging strategies proposed by the ideas of Lévy flight and Brownian motion. The MPA randomly initializes the prey location, updates the prey location through three foraging strategies, and finally overcomes the prematurity problem according to the FADs or vortex effect. The foraging strategy and the effect of FADs are described as follows:

(1) When the current iteration number is less than 1/3 of the maximum iteration number, the algorithm performs a global search by Brownian motion and updates the position of Prey according to Equation (33):

$$\begin{cases} \text{stepsize}_i = R_B \otimes (\text{Elite}_i - R_B \otimes \text{Prey}_i) \\ \text{Prey}_i = \text{Prey}_i + P \cdot R \otimes \text{stepsize}_i \end{cases} \tag{33}$$

where stepsize is the moving step of the prey; RB is a normally distributed Brownian random vector; Elite_i is the elite matrix; Prey_i is the prey matrix; $\otimes$ is the term-by-term multiplication operator; P is equal to 0.5; and R is the rand() function.

(2) When the current number of iterations is greater than 1/3 and less than 2/3 of the maximum number of iterations, the strategy of Lévy flight in parallel with Brownian motion is used to update the position of Prey, as shown in Equations (34) and (35).

$$\begin{cases} \text{stepsize}_i = R_L \otimes (\text{Elite}_i - R_L \otimes \text{Prey}_i) \\ \text{Prey}_i = \text{Prey}_i + P \cdot R \otimes \text{stepsize}_i \end{cases} \quad i = 1, 2, \cdots, \frac{n}{2} \tag{34}$$

$$\begin{cases} \text{stepsize}_i = R_B \otimes (R_B \otimes \text{Elite}_i - \text{Prey}_i) \\ \text{Prey}_i = \text{Elite}_i + P \cdot CF \otimes \text{stepsize}_i \end{cases} \quad i = \frac{n}{2} + 1, \cdots, n \tag{35}$$

where R_L is a random number with a Lévy distribution; $CF = (1 - \text{Iter}/\text{MaxIter})^{(2 \cdot \text{Iter}/\text{MaxIter})}$; and n is the number of prey.

(3) When the current number of iterations exceeds 2/3 of the maximum number of iterations, the algorithm updates Prey based on the Lévy motion strategy, as shown in Equation (36).

$$\begin{cases} \text{stepsize}_i = R_L \otimes (R_L \otimes \text{Elite}_i - \text{Prey}_i) \\ \text{Prey}_i = \text{Elite}_i + P \cdot CF \otimes \text{stepsize}_i \end{cases} \quad i = 1, 2, \cdots, n \tag{36}$$

(4) Finally, the algorithm overcomes the premature convergence problem through the vortex effect or fish aggregation devices (*FADs*) effect, as shown in Equation (37).

$$\text{Prey}_i = \begin{cases} \text{Prey}_i + CF[X_{min} + R_L \otimes (X_{max} - X_{min})] \otimes U, r \leq FADs \\ \text{Prey}_i + [FADs \cdot (1 - r) + r](\text{Prey}_{r1} - \text{Prey}_{r2}), r > FADs \end{cases} \tag{37}$$

where *FADs* (=0.2) is the probability of influencing the search process; U is a binary vector; r is a random number in the range of $[0, 1]$; and r_1 and r_2 are the index subscripts of the prey.

The support stiffness of the gears in a coaxial face gear split-torque transmission system has considerable influence on the load distribution and power flow [34,37]. The load-sharing coefficient usually expresses the balance of the load distribution; the larger the load-sharing coefficient, the more uneven the load distribution. In this study, we defined the load-sharing coefficients at Input Gears 1 and 2 and between the idler gears as:

$$\kappa_{in1} = max\left(\frac{2(max(F_{n16}, F_{n17}))}{F_{n16} + F_{n17}}\right) \tag{38}$$

$$\kappa_{in2} = max\left(\frac{2(max(F_{n26}, F_{n27}))}{F_{n26} + F_{n27}}\right) \tag{39}$$

$$\kappa_{id} = max\left(\frac{2(max(F_{n36}, F_{n46}))}{F_{n36} + F_{n46}}\right) \tag{40}$$

With the support stiffness of the pinions and the upper and lower face gears as parameters and the load-sharing coefficient as the target, the mathematical model for optimizing the load-sharing performance of the CFGSTTS was constructed as follows:

$$\begin{cases} F(\zeta_{in1}, \zeta_{in2}, \zeta_{id1}, \zeta_{id2}, \zeta_t, \zeta_l, \zeta_u) = \min(\kappa_{in1} + \kappa_{in2} + \kappa_{id}) \\ subject \ to \ 0.1 \leq \zeta_i \leq 10, i = in1, in2, id1, id2, t, l, u \end{cases} \tag{41}$$

where F denotes the nonlinear mapping of the support stiffness to the optimization objective; ζ_{in1} and ζ_{in2} denote the support stiffness factors of Input Gears 1 and 2, respectively; ζ_{id1}, ζ_{id2}, and ζ_t are the support stiffness factors of Idler 1, Idler 2, and the tail gear, respectively; and ζ_l and ζ_u represent the support stiffness factors of the lower and the upper face gear, respectively.

3. Verification

Accurate calculation of the meshing force for each gear pair is the premise of load-sharing behavior analysis. Figure 13 shows the meshing force comparison between the proposed model and the finite element model previously established [38]. The load of a single input gear is 1256 Nm. Inertia and damping were ignored in the calculation to facilitate comparison with the model in the literature [38].

Figure 13 shows that the maximum difference between the mean values of the meshing forces calculated by the two models is that of the meshing pair of Input Gear 2 and the lower face gear, which is 6.9%. However, the trend in the meshing force curve is the same. This is mainly because the torsional stiffness of the upper face gear web along the x and y axes was not included in the meshing stiffness calculation. The load-sharing coefficients of Input Gear 1, Input Gear 2, and the idler gear calculated by the proposed model are 1.2386, 1.2593, and 1.0761, respectively, while the load-sharing coefficients calculated by the finite element model are 1.2457, 1.2376, and 1.0620, respectively. The relative errors are 1.33%, 1.75%, and 1.33%, respectively. Therefore, the proposed model not only meets the accuracy requirements, but it can also substantially reduce the calculation time and provides a basis for analyzing the influence of parameters on the load-sharing behavior through many examples.
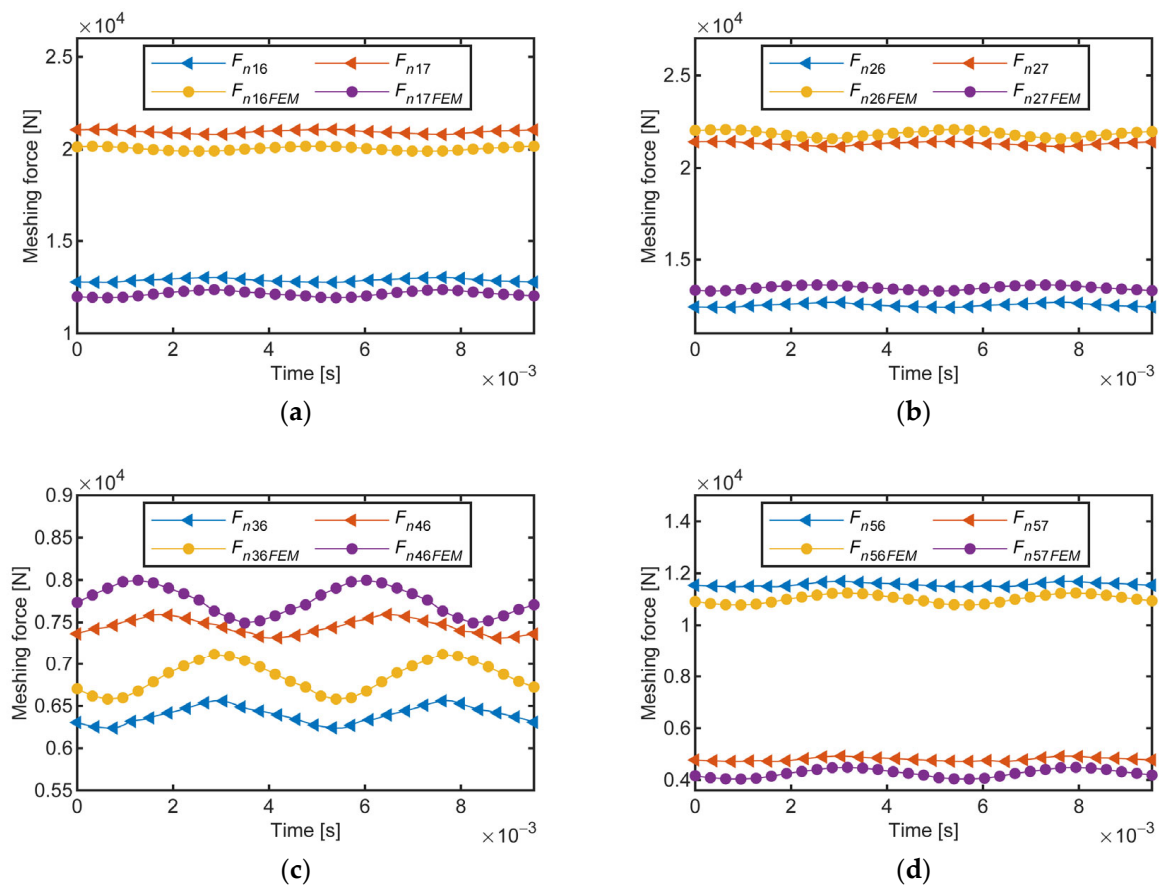
Figure 13. Comparison of meshing force between proposed model and finite element model: (**a**) Input Gear 1; (**b**) Input Gear 2; (**c**) idlers; (**d**) tail gear.

4. Numerical Results and Discussion

The dynamic differential Equations (26)–(32) of the CFGSTTS contain nonlinear factors, such as time-varying meshing stiffness, transmission error, and backlash, which are difficult to solved with analytical methods. Therefore, we used the variable-step Runge–Kutta method to calculate each gear pair's dynamic meshing force. The integration step length and integration time were $T_m/300$ and $200T_m$, respectively. The dynamic parameters and support stiffnesses used in this study are shown in Tables 2 and 3, respectively.

Table 3. Dynamic parameters of the face gear transmission system.

System Parameter	Symbol/Unit	Value
Mass of pinion	m_p/kg	1.95
Mass of face gear	m_6/kg	19.95
	m_7/kg	48.80
Inertia moment of pinion	J_p/kg·m^2	2.31×10^{-3}
Inertia moment of face gear	J_{6x}, J_{6y}/kg·m^2	0.84
	J_{6z}/kg·m^2	1.49
	J_{7x}, J_{7y}/kg·m^2	1.52
	J_{7z}/kg·m^2	2.48
Supporting damping of pinion	c_{px}, c_{py}/N·s·m^{-1}	0.8×10^4

Table 3. *Cont.*

System Parameter	Symbol/Unit	Value
Supporting damping of face gear	$c_{6x}, c_{6y}, c_{6z}/\text{N·s·m}^{-1}$	1.2×10^4
	$c_{6\theta x}, c_{6\theta y}/\text{N·m·s·rad}^{-1}$	0.9×10^4
	$c_{7x}, c_{7y}, c_{7z}/\text{N·s·m}^{-1}$	1.2×10^4
	$c_{7\theta x}, c_{7\theta y}/\text{N·m·s·rad}^{-1}$	0.9×10^4
Damping ratio	ξ	0.05
Normal gear backlash	b_{h}/mm	0.02
Static transmission error	e_0/mm	0
	e_{r}/mm	0.01

4.1. Influence of Support Stiffness on Load-Sharing Coefficient under Different Loads

To study the effects of the support stiffness and input load on the load-sharing characteristics of the coaxial face gear split-torque transmission system, the dynamics were analyzed under dual-input and dual-output operating conditions. The input torque T_{in} for a single input gear varied between 500 and 1500 Nm, and the support stiffness factor ζ_i ($i = in1, in2, id1, id2, t, l, u$) for each gear ranged from 0.1 to 10. While analyzing the effect of the support stiffness of a single gear on the load-sharing factor for a given load, the support stiffness of the remaining gears was fixed.

The influence of the support stiffness of Input Gear 1 on the load sharing under various loads was investigated. In Figure 14a, the value of the load-sharing coefficient κ_{in1} in the upper left region is the largest, which indicates that increasing the support stiffness and decreasing the load increase κ_{in1}. Similar to prior results [38], the support stiffness of the input gear has a stronger effect on the load-sharing behavior of the input gear. However, the distribution of the load-sharing coefficient in Figure 14b is different from that in Figure 14a. As the support stiffness changes from 0.1 to 10, the load-sharing coefficient κ_{in2} shows an overall decreasing trend. In addition, Figure 14c shows that the smaller support stiffness of Input Gear 1 is more favorable for load equalization between the idlers.
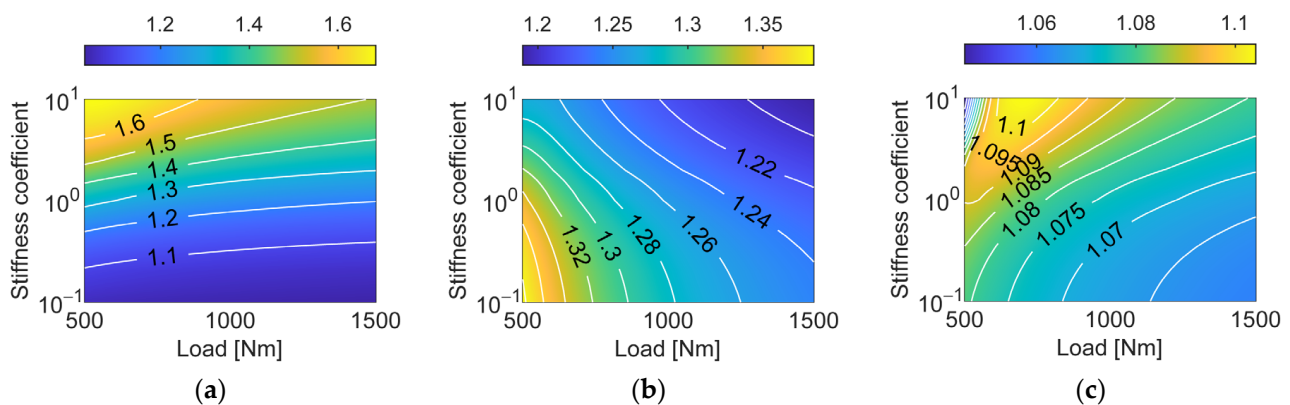

Figure 14. Influence of support stiffness of Input Gear 1 on load-sharing coefficient: (**a**) Input Gear 1; (**b**) Input Gear 2; (**c**) idler gear.

Figure 15 illustrates the effect of the support stiffness of Input Gear 2 on the load sharing at different input loads. Figure 15a shows that the value of the load-sharing coefficient κ_{in1} in the lower left corner is the largest and then gradually decreases with increasing support stiffness and load. The heatmap distribution of the load-sharing coefficient in Figure 15b is similar to that in Figure 14a, and the influence of the support stiffness of Input Gear 2 on κ_{in2} is more apparent. The effect of the support stiffness of Input Gear 2 on κ_{id} is similar to that shown in Figure 14c, indicating that κ_{id} decreases with a higher load and increases with a larger support stiffness.
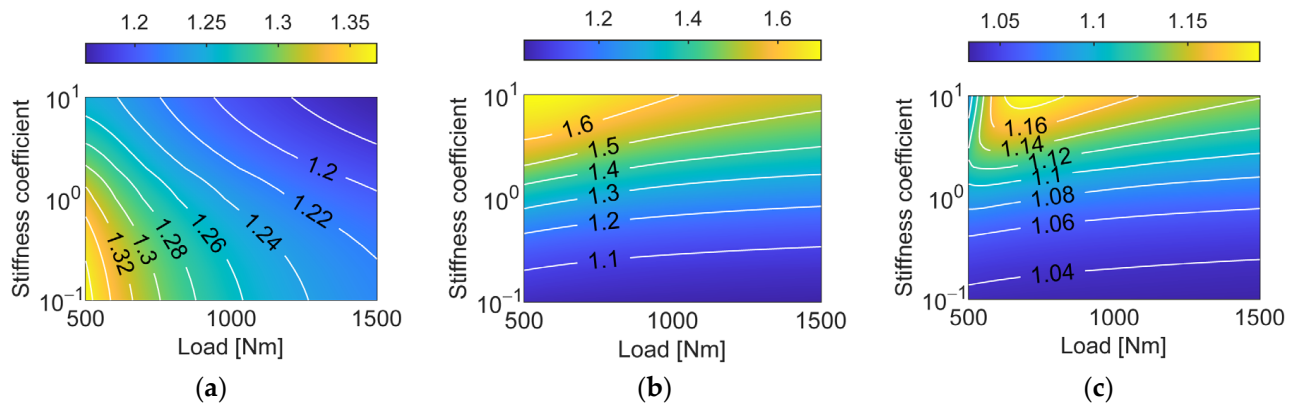
Figure 15. Influence of support stiffness of Input Gear 2 on load-sharing coefficient: (**a**) Input Gear 1; (**b**) Input Gear 2; (**c**) idler gear.

Then, the change in the load-sharing coefficient with changes in the support stiffness of Idlers 1 and 2 is revealed in Figures 16 and 17. The thermal diagram and contour distribution of the load-sharing coefficient in Figure 16a, 16b, and 16c are similar to those in Figure 17a, 17b, and 17c, respectively, with only a slight difference in the numerical value. In other words, the variation in the support stiffness of Idlers 1 and 2 has a similar effect on κ_{in1}, κ_{in2}, and κ_{id}. Notably, the effect of the idler support stiffness on κ_{id} is more prominent. Therefore, a smaller support stiffness of the idlers results in a more uneven load distribution. The higher the support stiffness of the idlers, the more balanced the load of the input gear. However, excessive support stiffnesses ζ_{id1} and ζ_{id2} increase the load-sharing coefficient κ_{id}. Therefore, from the perspective of load equalization, choosing the support stiffness at the idlers needs further analysis. Additionally, the influence trend of the support stiffness of the idler gear on the load-sharing coefficient of the input gear is similar to that previously reported [37,38].
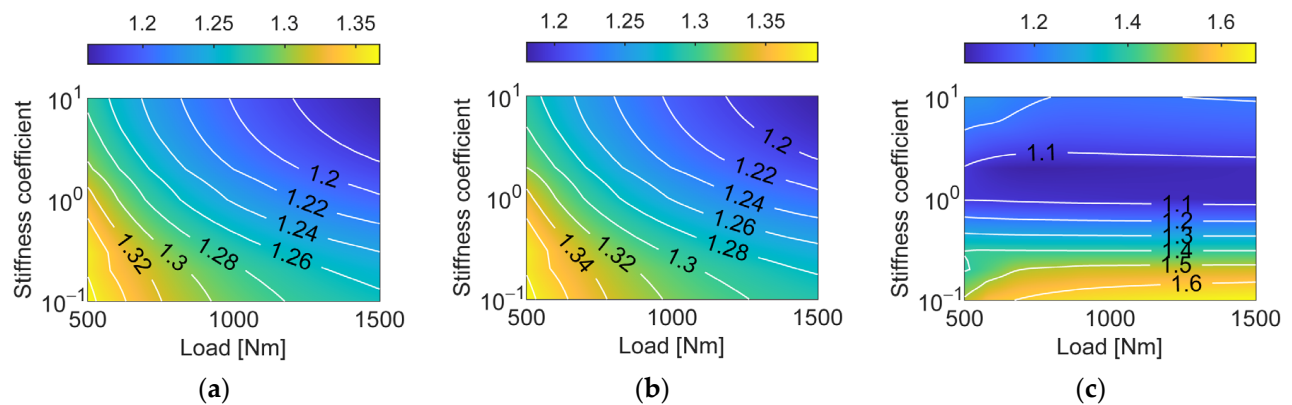

Figure 16. Influence of support stiffness of Idler 1 on load-sharing coefficient: (**a**) Input Gear 1; (**b**) Input Gear 2; (**c**) idler gear.
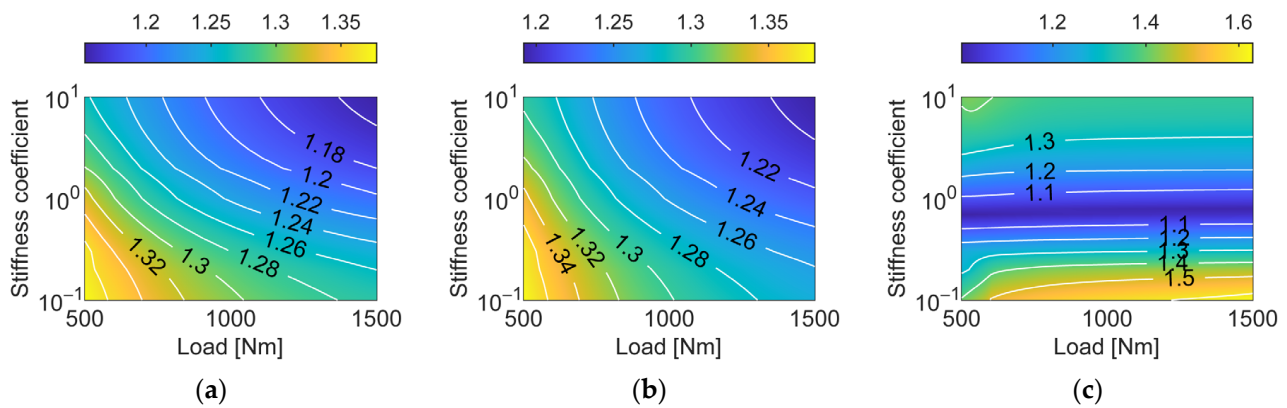
Figure 17. Influence of support stiffness of Idler 2 on load-sharing coefficient: (**a**) Input Gear 1; (**b**) Input Gear 2; (**c**) idler gear.

Figure 18 shows the contour distribution of the load-sharing coefficient under different support stiffnesses of the tail gear and input loads. The distribution of the contours in the three subplots is nearly the same, indicating that the support stiffness of the tail gear has a similar effect on κ_{in1}, κ_{in2}, and κ_{id}. By increasing the support stiffness of the tail gear at a specific input load, the load-sharing coefficients κ_{in1}, κ_{in2}, and κ_{id} decrease to varying degrees. Consequently, a higher support stiffness of the tail gear is conducive to lowering the load-sharing factor and balancing the load carrying of each meshing pair.
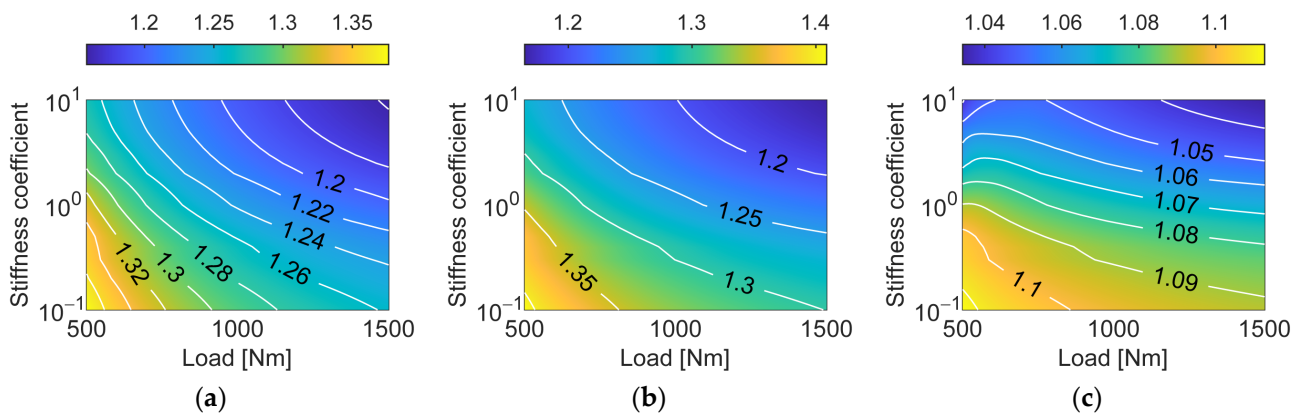

Figure 18. Influence of support stiffness of tail gear on load-sharing coefficient: (**a**) Input Gear 1; (**b**) Input Gear 2; (**c**) idler gear.

Figures 19 and 20 depict the influence of the support stiffness of the lower and upper face gears, respectively, on the load sharing. As shown in Figure 19, an increase in the support stiffness of the lower face gear yields a more balanced load distribution at the input gear, but the load nonuniformity of the two idlers slightly increases. Overall, a higher support stiffness of the lower face gear is more appropriate for the load sharing of the system. A comparison of Figures 19 and 20 reveals that the support stiffness of the upper face gear has a more complex effect on the load sharing than that of the lower face gear. Higher the support stiffness of the upper face gear ζ_u increases the load-sharing coefficient of Input Gear 1, thus aggravating the uneven load distribution at Input Gear 1. Nevertheless, the increase in ζ_u benefits the load balance of the idlers. In summary, the change in the support stiffness of the upper face gear, to a certain extent, can adjust the balance load condition of the system, but it must be matched with the support stiffness of other gears.
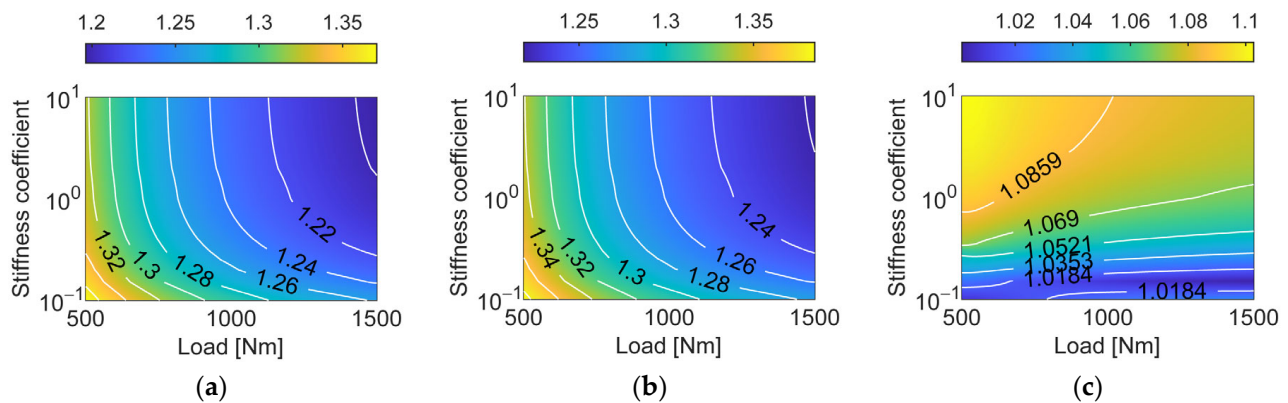
Figure 19. Influence of support stiffness of lower face gear on load-sharing coefficient: (**a**) Input Gear 1; (**b**) Input Gear 2; (**c**) idler gear.
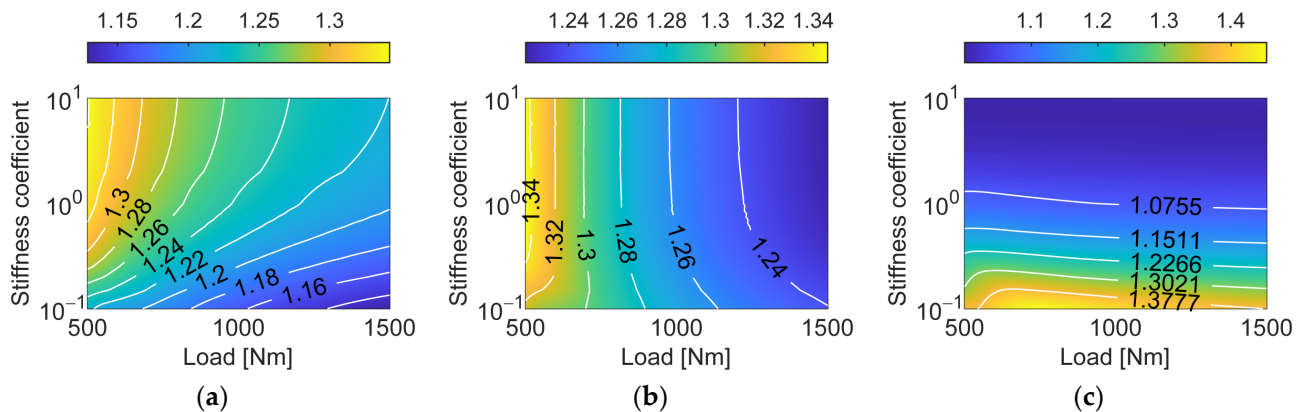

Figure 20. Influence of support stiffness of upper face gear on load-sharing coefficient: (**a**) Input Gear 1; (**b**) Input Gear 2; (**c**) idler gear.

4.2. Optimization Analysis

The established optimization model was solved through the marine predator algorithm. The load of a single input gear was 800 Nm. The other dynamic parameters are listed in Tables 2 and 3. The number of prey and maximum number of iterations were set to 80 and 100, respectively, to reduce the computational scale of the optimization algorithm. Then, the computation was accelerated by parallel settings. The convergence curve of the algorithm is shown in Figure 21. We found a sufficient decrease in the function value around ten iterations, which also indicated that the marine predator algorithm had a fast convergence rate.
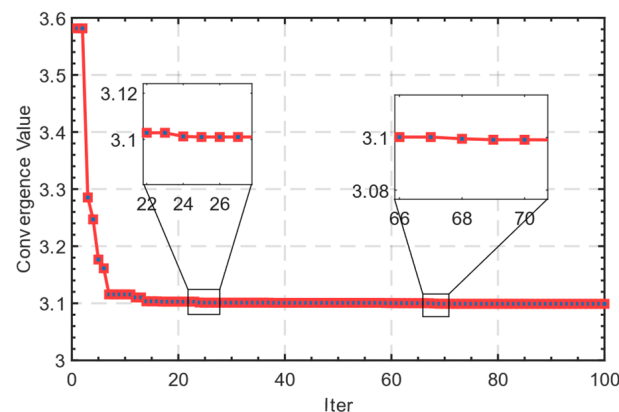

Figure 21. Convergence curve.

Table 4 presents the optimized support stiffness coefficients for each gear. The load-sharing coefficients of Input Gears 1 and 2 and the idler before optimization were 1.375, 1.388, and 1.046, respectively; after optimization, they were 1.049, 1.052, and 1.000, respectively. We noted a marked reduction in the load-sharing coefficients of Input Gears 1 and 2. To more clearly show the effect of optimization, the meshing force of each pinion with the upper and lower face gears was calculated separately, as shown in Figure 22, with OPT indicating the optimized meshing force. As shown in Figure 22a, the meshing force between Input Gear 1 and the upper gear was reduced, and the average value was reduced from 14,830 N before optimization to 11,320 N. As the meshing force between Input Gear 1 and the lower face gear increased, the average value rose from 6730 to 10,240 N, leading the meshing forces Fn16 and Fn17 to be close. This indicated that more power from Input Gear 1 flowed to the lower face gear. Figure 22b presents the change in the meshing force of Input Gear 2 with the upper and lower face gears before and after optimization, with a similar law as that shown in Figure 22a. Figure 22c,d show that the mean value of the meshing force of the idlers with the upper and lower face gears appeared to increase after optimization, but its mean load factor slightly decreased. This is because the power transmitted from Input Gears 1 and 2 to the lower face gear increased, and the increased power was transmitted to the upper face gear through the idlers.

Table 4. Values of optimized support stiffness coefficients.

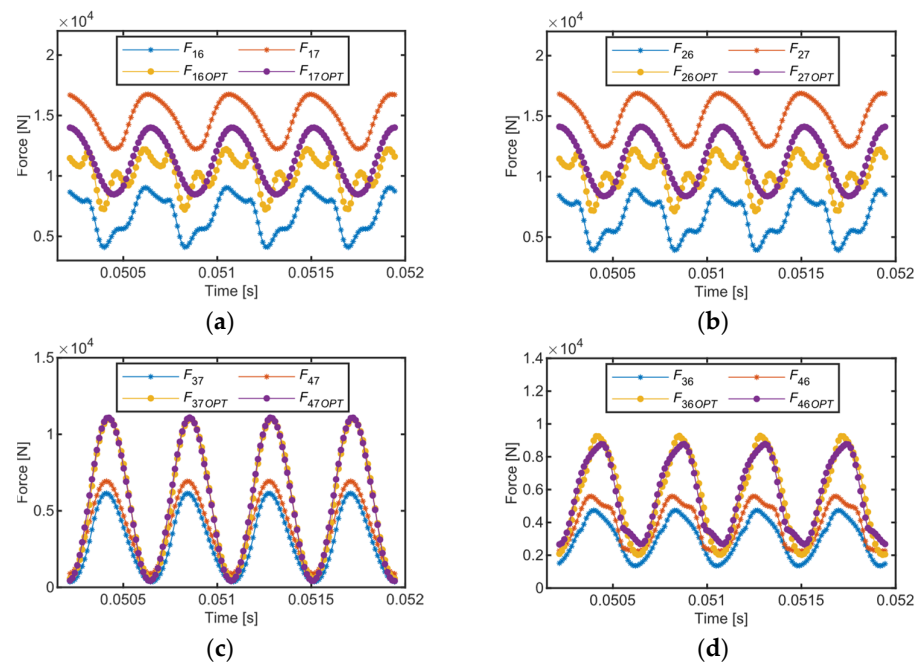| Parameter	ζ_{in1}	ζ_{in2}	ζ_{id1}	ζ_{id2}	ζ_t	ζ_l	ζ_u
Value	0.10	0.10	6.32	9.99	3.82	0.58	5.93

Figure 22. Dynamic meshing force curve before and after optimization: (**a**) Input Gear 1; (**b**) Input Gear 2; (**c**) idler gear–upper face gear; (**d**) idler gear–lower face gear.

To verify the validity of the optimized model, the meshing forces of the gear pair before and after optimization were compared with a previously established quasistatic finite element analysis model [38], as shown in Figure 23. The load of a single input gear was 1256 Nm. Similar to the dynamic meshing force, the static meshing force of Input Gears 1 and 2 with the upper face gear substantially decreased at the optimized support stiffness, while the meshing force with the lower face gear increased. In addition, the average meshing force of Idlers 1 and 2 changed from 6850 N and 7750 N to 10,560 N and 10,680 N, respectively. Thus, the load-sharing coefficient at the idler reduced. We

sufficiently demonstrated that the load was more evenly distributed among the gear pairs with the optimized support stiffness.
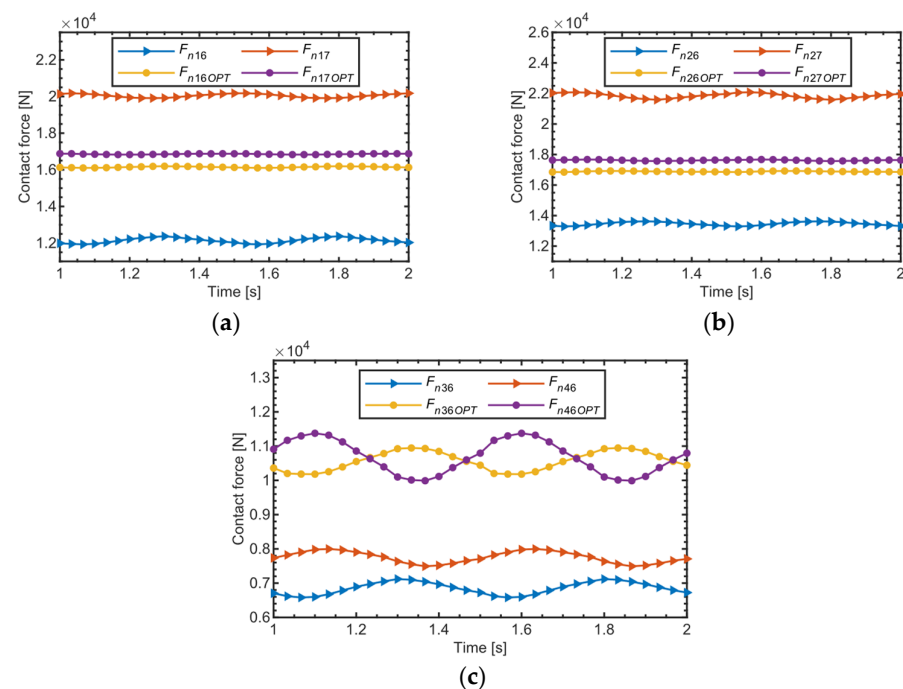

Figure 23. Meshing force of each gear pair by finite element method: (**a**) Input Gear 1; (**b**) Input Gear 2; (**c**) idlers.

5. Conclusions

A dynamic load-sharing model of a dual-input, dual-output, concentric gear split-torque system was established, which considered the translational and torsional vibration of gears. The correlation between the meshing stiffness and load was considered. Then, a time-varying meshing stiffness agent model was developed based on a feedforward neural network. According to the power flow characteristics of this system, two meshing states, pinion driving and face gear driving, were considered. The load-sharing characteristic analysis and optimization were completed in this study. The conclusions drawn from the study can be summarized as follows:

(1) The results showed that reducing the support stiffness of Input Gear 1 decreases the load-sharing coefficients. Increasing the support stiffness of the tail gear increases the load-sharing capacity. Furthermore, the support stiffness of the idlers, Input Gear 2, and upper and lower face gears have different effects on κ_{in1}, κ_{in2}, and κ_{id} and need to be comprehensively considered when adjusting the load-sharing performance.

(2) Based on the marine predator optimization algorithm, the load-sharing optimization model of the concentric gear split-torque transmission system was established. The optimization results showed that the load-sharing factor decreased from 1.375, 1.388, and 1.046 to 1.049, 1.052, and 1.000, respectively. Moreover, the optimization effect was verified by comparing the gear pair meshing force before and after optimization by the finite element method.

(3) The analysis results showed that the load distribution of the gears can be more balanced by the support structure and the design of the support bearings. Therefore, the optimized support stiffness coefficients have practical importance for the design of each support bearing, as well as the support structure.

References

1. White, G. Helicopter transmission arrangements with split-torque gear trains. In *NASA. Lewis Research Center Advanced Power Transmission*; Transmission Research, Inc.: Cleveland, OH, USA, 1983.
2. Kish, J.G. *Sikorsky Aircraft Advanced Rotorcraft Transmission (ART) Program-Final Report*; NASA CR-191079; NASA Lewis Research Center: Washington, DC, USA, 1993.
3. Krantz, T.L. Dynamics of a Split Torque Helicopter Transmission. Master's Thesis, Cleveland State University, Cleveland, OH, USA, 1994.
4. Krantz, T.L.; Rashidi, M.; Kish, J.G. Split torque transmission load sharing. *Proc. Inst. Mech. Eng. Part G J. Aerosp. Eng.* **1992**, *208*, 137–148. [CrossRef]
5. Heath, G.F.; Bossler, R.B., Jr. *Advanced Rotorcraft Transmission (ART) Program-Final Report*; National Aeronautics and Space Administration: Washington, DC, USA, 1993; pp. 1–206.
6. Lewicki, D.G.; Handschuh, R.F.; Heath, G.F. Evaluation of Carburized and ground Face Gears. *J. Am. Helicopter Soc.* **2000**, *45*, 118–124. [CrossRef]
7. Lewicki, D.G.; Heath, G.F.; Filler, R.R.; Slaughter, S.C.; Fetty, J. RDS-21 face-gear surface durability tests. In Proceedings of the American Helicopter Society 63rd Annual Forum, Virginia Beach, VA, USA, 1–3 May 2007.
8. Lewicki, D.G.; Dempsey, P.J.; Heath, G.F. Gear Fault Detection Effectiveness as Applied to Tooth Surface Pitting Fatigue Damage. In Proceedings of the American Helicopter Society 65th Annual Forum, Grapevine, TX, USA, 27–29 May 2009.
9. Heath, G.F.; Slaughter, S.C.; Fisher, D.J. Helical face gear development under the enhanced rotorcraft drive system program. In Proceedings of the 67th Annual Forum and Technology Display (Forum 67), Virginia Beach, VA, USA, 3–5 May 2011. (AHS 2011-000270).
10. Kish, J. Comanche drive system. In Proceedings of the American Helicopter Society Rotary Wing Propulsion Specialists Meeting, Williamsburg, VA, USA, 25–28 October 1993.
11. Heath, G.F.; Slaughter, S.C.; Morris, M.T. Face gear development under the rotorcraft drive system for the 21st century program. In Proceedings of the 65th Annual Forum Proceedings-AHS International, Grapevine, TX, USA, 27–29 May 2009; Volume 2, pp. 1011–1030.
12. Mo, S.; Yue, Z.X.; Feng, Z.Y. Analytical investigation on load sharing characteristics for face gear split flow system. *J. Huazhong Univ. Sci. Technol. Nat. Sci. Ed.* **2020**, *48*, 23–28. (In Chinese) [CrossRef]
13. Zhao, N.; Wang, R.F.; Tao, L. Load Sharing of Parallel Shaft Split Torque Transmission System. *Adv. Mater. Res.* **2012**, *490–495*, 2231–2235. [CrossRef]
14. Dong, H.; Duan, L.L.; Zhang, J.A. Load-Sharing Characteristics of Power-Split Transmission System Based on Deformation Compatibility and Loaded Tooth Contact Analysis. *Int. J. Aerosp. Eng.* **2015**, *2015*, 305808. [CrossRef]
15. Fu, C.X.; Zhao, N.; Zhao, Y.Z. Load Sharing Multiobjective Optimization Design of a Split Torque Helicopter Transmission. *Math. Probl. Eng. Theory Methods Appl.* **2015**, *2015 Pt 20*, 381010. [CrossRef]
16. Dong, H.; Liu, Z.Y.; Zhao, X.L.; Hu, Y.H. Research on static load sharing characteristics of power split two-stage five-branching star gearing drive system. *J. Vibroeng.* **2019**, *21*, 11–27. [CrossRef]
17. Hu, Z.; Tang, J.; Wang, Q. Investigation of nonlinear dynamics and load sharing characteristics of a two-path split torque transmission system. *Mech. Mach. Theory* **2020**, *152*, 103955. [CrossRef]
18. Liu, X.; Fang, Z.D.; Jia, H.; Zhao, N.; Sheng, Y. Investigation of Load Sharing and Dynamic Load Characteristics of a Split Torque Transmission System with Double-Helical Gear Modification. *Shock. Vib.* **2021**, *2021*, 9912148. [CrossRef]
19. Jin, G.H.; Yang, H.Y.; Zhu, R.P. Tooth surface friction and its influence on dynamic transmission error of double power input transmission system. *J. Vibroeng.* **2018**, *20*, 1937–1954. [CrossRef]
20. Jin, G.H.; Xiong, Y.P.; Gui, Y.F.; Zhu, R.P. Sensitive Parameter and Its Influence Law on Load Sharing Performance of Double Input Split Torque Transmission System. *J. Vib. Eng. Technol.* **2017**, *5*, 583–595.
21. Lin, T.J.; Ran, X.T. Nonlinear vibration characteristic analysis of a face-gear drive. *J. Vib. Shock.* **2012**, *31*, 25–31.

22. Litvin, F.L.; Zhang, Y.; Wang, J.; Bossler, R.B.; Chen, Y.D. Design and Geometry of Face-Gear Drives. *J. Mech. Des.* **1992**, *114*, 642–647. [CrossRef]

23. Litvin, F.L.; Egelja, A.; Tan, J.; Heath, G. Computerized design, generation and simulation of meshing of orthogonal offset face-gear drive with a spur involute pinion with localized bearing contact. *Mech. Mach. Theory* **1998**, *33*, 87–102. [CrossRef]

24. Litivin, F.L.; Alfonso, F.; Laudio, Z.Z. Design, generation and TCA of new type of asymmetric face-gear drive with modified geometry. *Comput. Methods Appl. Mech. Eng.* **2001**, *190*, 5837–5865. [CrossRef]

25. Litvin, F.L.; Nava, A.; Fan, Q.; Fuentes, A. New geometry of worm face gear drives with conical and cylindrical worms: Generation, simulation of meshing, and stress analysis. *Comput. Methods Appl. Mech. Eng.* **2002**, *191*, 3035. [CrossRef]

26. Handschuh, R.F.; Lewicki, D.G.; Heath, G.F. *Experimental Evaluation of Face Gears for Aerospace Drive System Applications*; National Aeronautics and Space Administration Cleveland Oh Lewis Research Center: Cleveland, OH, USA, 1996.

27. Handschuh, R.F.; Lewicki, D.G.; Bossler, R.B. Experimental testing of prototype face gears for helicopter transmissions. *Proc. Inst. Mech. Eng.* **1994**, *208*, 129. [CrossRef]

28. Pias, R.; Turro, S. Face-Gear Transmission Assembly with Floating Balance Pinions. U.S. Patent 5,974,911, 2 November 1999.

29. Jin, G.H.; Ren, W.; Zhu, R.P. Influence of backlash on load sharing and dynamic load characteristics of twice split torque transmission system. *J. Vib. Eng. Technol.* **2019**, *7*, 565–577. [CrossRef]

30. Mo, S.; Yue, Z.; Feng, Z.; Shi, L.; Zou, Z.; Dang, H. Analytical investigation on load-sharing characteristics for multi-power face gear split flow system. *Proc. Inst. Mech. Eng. Part C J. Mech. Eng. Sci.* **2020**, *234*, 676–692. [CrossRef]

31. Mo, S.; Song, Y.; Feng, Z. Research on dynamic load sharing characteristics of double input face gear split-parallel transmission system. *Proc. Inst. Mech. Eng. Part C J. Mech. Eng. Sci.* **2022**, *236*, 2185–2202. [CrossRef]

32. Dong, J.; Hu, Z.; Tang, J. Investigation of the Vibration Features and Dynamic Load Sharing Characteristics of Concentric Face Gear Torque Split Transmission. *J. Comput. Nonlinear Dyn.* **2021**, *16*, 071003. [CrossRef]

33. Zhao, N.; Li, W.; Hu, T. Quasistatic load sharing behaviours of concentric torque-split face gear transmission with flexible face gear. *Math. Probl. Eng.* **2018**, *2018*, 6568519. [CrossRef]

34. Dong, J.; Wang, Q.; Tang, J. Dynamic characteristics and load-sharing performance of concentric face gear split-torque transmission systems with time-varying mesh stiffness, flexible supports and deformable shafts. *Meccanica* **2021**, *56*, 2893–2918. [CrossRef]

35. Gong, F.; Zhu, R.P.; Li, P.J. Analysis of Nonlinear Vibration Characteristics of the Concentric Face-Gear Split-Torque Transmission System. *Math. Probl. Eng.* **2022**, *2022*, 1977367. [CrossRef]

36. Faramarzi, A.; Heidarinejad, M.; Mirjalili, S. Marine Predators Algorithm: A nature-inspired metaheuristic. *Expert Syst. Appl.* **2020**, *152*, 113377. [CrossRef]

37. Li, W.; Zhao, N.; Lin, Y.H.; Qiu, P.Y. Study on Dynamic Load Sharing Characteristics of the Concentric Torque Split Face Gear Transmission. *J. Xi'an Jiaotong Univ.* **2020**, *54*, 1–9. (In Chinese)

38. Gong, F.; Zhu, R.; Li, P. Analysis of Load-Sharing and Contact Characteristics of the Concentric Face Gear Split-Torque Transmission System with Elastic Supports. *Appl. Sci.* **2022**, *12*, 4894. [CrossRef]